Motion Primitives and Control on a Spherical Surface with Application to Tethered Aircraft

Sérgio Vinha SYSTEC-ISR ARISE, Faculdade de Engenharia, Universidade do Porto, Rua Dr. Roberto Frias, 4200-465 Porto, Portugal. svinha@fe.up.pt

Gabriel M. Fernandes SYSTEC-ISR ARISE, Faculdade de Engenharia, Universidade do Porto, Rua Dr. Roberto Frias, 4200-465 Porto, Portugal. gmfernandes@fe.up.pt

Manuel C.R.M. Fernandes SYSTEC-ISR ARISE, Faculdade de Engenharia, Universidade do Porto, Rua Dr. Roberto Frias, 4200-465 Porto, Portugal. mcrmf@fe.up.pt

Fernando A.C.C. Fontes SYSTEC-ISR ARISE, Faculdade de Engenharia, Universidade do Porto, Rua Dr. Roberto Frias, 4200-465 Porto, Portugal. faf@fe.up.pt

ABSTRACT

This paper proposes the use of motion primitives on a spherical surface for controlling tethered aircraft. A fundamental constraint of tethered aircraft motion is the restriction to move on a spherical surface. This leads to complex dynamics which are challenging to control, especially during take-off and landing maneuvers. To address this issue, we utilize motion primitives, predefined motion patterns that simplify trajectory control design. By formulating the control problem in a cylindrical coordinate framework associated with the motion primitives, we leverage the minimal influence of periodic variables to enable linearized control models that can comply with demanding requirements. A dynamical model and control architecture are developed, enabling the use of standard multivariable control techniques. Simulations confirm the effectiveness of the approach, demonstrating accurate reference tracking and smooth transitions between primitives, highlighting their potential for tethered aircraft control, especially in airborne wind energy systems.

Keywords: Motion Primitives; Airplane Control; Tethered Aircraft; Kite Control; Unmanned Aerial Vehicles (UAVs); Airborne Wind Energy.

Nomenclature

A, b	=	wing area $\left[\mathrm{m}^2\right]$, and wingspan $[\mathrm{m}]$
$c_\mathrm{D}, c_\mathrm{L}$	=	aerodynamic drag and lift coefficients
$\mathbf{F}_\mathrm{D}, F_\mathrm{D}$	=	aerodynamic drag vector and magnitude $[\mathrm{N}]$
$\mathbf{F}_\mathrm{L}, F_\mathrm{L}$	=	aerodynamic lift vector and magnitude $[\mathrm{N}]$
$\mathbf{F}_\mathrm{p}, F_\mathrm{p}$	=	propeller thrust vector and magnitude $[\mathrm{N}]$
$\mathbf{F}_\mathrm{i}, F_\mathrm{i}$	=	inertial force vector and magnitude $[\mathrm{N}]$
$\mathbf{F}_\mathrm{t}, F_\mathrm{t}$	=	tether force vector and magnitude $[\mathrm{N}]$
g	=	gravitational acceleration $\left[\mathrm{m\,s}^{-2}\right]$
m	=	mass $\left[\mathrm{kg}\right]$

ρ_a	=	air density $\left[\mathrm{kg\,m^{-3}}\right]$
V	=	vehicle speed $\left[\mathrm{m\,s^{-1}}\right]$
$\mathbf{p}$	=	aircraft position [m]
$\mathbf{V}, V$	=	aircraft velocity vector and magnitude $\left[\mathrm{m\,s^{-1}}\right]$
$\mathbf{V_a}, V_a$	=	aircraft airspeed vector and magnitude $\left[\mathrm{m\,s^{-1}}\right]$
$\mathbf{V_w}, V_w$	=	wind velocity vector and magnitude $\left[\mathrm{m\,s^{-1}}\right]$
$\mathbf{X}, \mathbf{U}$	=	state and control vectors in the simulation model
(r, φ, β)	=	spherical coordinates: sphere radius [m], azimuth angle [rad], fx elevation angle [rad]
(ρ, σ, h)	=	cylindrical coordinates: radial distance [m], angular position[rad], height [m]
α, γ	=	angle-of-attack and flight-path angle [°, rad]
ϕ, θ, ψ	=	roll, pitch and yaw angles [°, rad]
$\omega_p, \omega_q, \omega_r$	=	roll, pitch and yaw rates $\left[^\circ\,\mathrm{s^{-1}}, \mathrm{rad\,s^{-1}}\right]$

1 Introduction

In recent years, research on tethered aircraft has gained increasing attention [1]. Their ability to operate reliably in sensitive or regulated areas makes them well-suited for applications such as telecommunications, surveillance, environmental monitoring, emergency response, and electricity generation. Additionally, their sustained and controlled operation under various conditions enhances their versatility. The motion of tethered aircraft (assuming a stretched tether with constant length) is constrained to the surface of a sphere. Such constraints present control challenges, mainly when trying to address the problem with model-based real-time implementable control methods.

A key application of tethered aircraft is in Airborne Wind Energy Systems (AWES), where kites or drones are used to harvest wind energy at high altitudes, where wind speeds are stronger and more consistent [2]. There has been a considerable research effort from the control community in addressing AWES [3]. However, some motion control, especially during the take-off and landing phases, presents significant control challenges due to the complex dynamics of tethered flight [4]. One promising approach to overcoming these challenges is the use of circular trajectories for take-off and landing [5, 6]. These trajectories enable smoother transitions, reduce mechanical stress on the tether, and improve the system's stability and operational safety.

Motion primitives provide a structured framework for decomposing complex maneuvers into manageable, predefined actions. Motion primitives are fundamental motion segments that allow a mechanical system to transition between states within its state space. Widely used in robotics, autonomous vehicles, and other systems requiring precise and coordinated movements, motion primitives play a significant role in motion planning and control. Their application to the control of tethered aircraft, in particular in the context of AWES, can enhance efficiency and reliability in challenging operational environments.

In this article, motion primitives on the surface of a sphere are explored in the context of control engineering. We introduce motion primitives, analyze their kinematics, and examine their application within control methodologies. The primary advantage of utilizing the motion primitives framework along with the cylindrical coordinate system is the simplicity it offers in designing a controller to guide the trajectory toward a reference path within a primitive. This is largely because in the proposed framework, the periodic variables have minimal influence on the system dynamics. A key consequence is that a simple linearized model around a point on the path provides a good approximation in the vicinity of the reference trajectory. As a result, implementing standard linear multivariable control methods for each primitive proves to be an effective control strategy, as demonstrated throughout the article.

The structure of this paper is as follows. We first introduce the nomenclature used throughout the work. Section 2 presents the concept of motion primitives on a spherical surface and explains how they

can be used to construct a reference path. Section 3 describes a core contribution of this paper: obtaining the dynamical model of a tethered aircraft in the appropriate framework to be used with the proposed motion primitives. Section 4 presents the control architecture used. In Section 5, simulation results are reported. These show the efficacy that can be obtained when using standard linear control methods combined with the proposed motion primitive framework. The concluding section, Section 6, highlights the effectiveness of motion primitives in this application.

2 Motion Primitives on spherical surfaces

Motion primitives are fundamental, predefined motion patterns that act as building blocks for generating complex movements. They are widely used in robotics and motion planning [7, 8], providing a structured approach to movement control. On a spherical surface, all motions inherently exhibit curvature, meaning that any continuous path can be represented as a combination of circular primitives. The proposed primitive framework [9] can effectively describe any spherical motion and can easily accommodate the constraints on limited curvature that are common in many vehicles.

2.1 Circular motion primitives on spherical surfaces

In this work, we are interested in describing motions on the surface of a sphere for control purposes. If we consider a sphere of radius r, any path on the sphere's surface has a curvature with a radius smaller or equal to r. We can then define a Motion Primitive on the surface of a sphere to be a circle. This circle can be obtained by intersecting the sphere with a plane π, that we call the path plane (see Fig. 1).

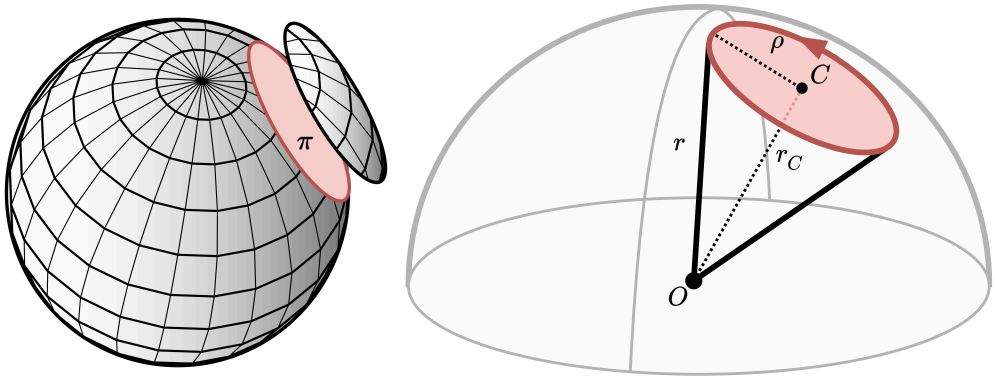

Fig. 1 Sphere cut by a plane, defining a circle with center C and radius ρ.

The intersection of the sphere with a secant plane π defines a circle with center C. The vector $\overrightarrow{OC}$ is orthogonal to the plane at C. Moreover, we have $r^2 = r_C^2 + \rho^2$, where r_C is the distance of C to the origin O and ρ is the radius of the circle.

The motion primitive path can be defined simply by defining the point C. This point is conveniently defined in spherical coordinates $(r_C, \varphi_C, \beta_C)$, where r_C is the distance to the sphere origin, φ_C is the azimuth angle, and β_C is the elevation angle (measured from the plane OXY). Using spherical coordinates, a radial vector can always be defined by φ_C and β_C, even when $r_C = 0$.

In summary, given a point C in spherical coordinates, it defines a circular path on the surface of the sphere, centered at C with radius $\rho = \sqrt{r^2 - r_C^2}$.

2.2 Kinematics of points in the motion primitive

We have seen that given a point C in spherical coordinates, we can define a spherical circular path centered at C. To define a point p in the circular path, we consider an additional parameter, its angular position $\sigma \in [0, 2\pi]$ (see Fig. 2).

The coordinates of p are given by

$$p = C + \rho \cos\sigma \, \overrightarrow{e}_{\varphi_C} + \rho \sin\sigma \, \overrightarrow{e}_{\beta_C}, \tag{1}$$

where p and C are in Cartesian coordinates and e_{φ_C} and e_{β_C} are the local orthogonal unit vectors in the directions of increasing φ and β at C. When σ equals to zero, the point p is at its most Eastern point in the path (p_0). If the vehicle is moving with speed V, the instantaneous angular velocity is $\omega_C = \frac{V}{\rho}$,which is positive if anticlockwise, when seen from outside the sphere (see Fig. 2).

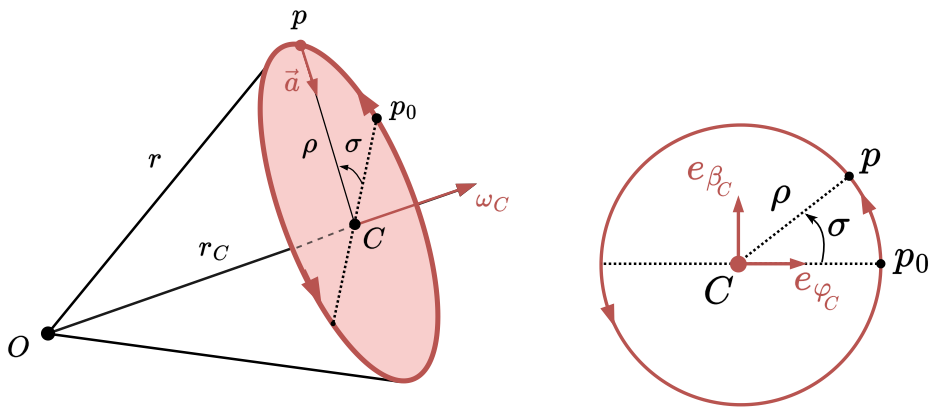

Fig. 2 Point p on the circle with angular position σ, with unit vectors $e_{\beta_C}, e_{\varphi_C}$. Angular velocity ω_C and centripetal acceleration a.

If the vehicle is at position p moving in the circle with constant speed V, then the acceleration is

$$\overrightarrow{a} = \frac{V^2}{||\overrightarrow{pC}||} \frac{\overrightarrow{pC}}{||\overrightarrow{pC}||} = \frac{V^2}{\rho^2} \overrightarrow{pC}, \tag{2}$$

with direction to the center of the curvature C. The acceleration can be used to compute the open-loop control to be used in the reference path/trajectory.

In order to control a vehicle to move in the motion primitive, it is convenient to consider a cylindrical coordinate frame centred at the point C and with symmetry axis e_{r_C}, having coordinates (ρ, σ, h). The coordinates comprise ρ – the radial distance from the point C, σ – the angular position from the circular path measured from the Eastmost point p_0, and h – the height measured from the path plane π.

In cylindrical coordinates, the position, velocity, and acceleration vectors are expressed as (see e.g. [10]):

$$\mathbf{p} = \begin{bmatrix} \rho \\ \sigma \\ h \end{bmatrix}, \quad \dot{\mathbf{p}} = \begin{bmatrix} \dot{\rho} \\ \rho\dot{\sigma} \\ \dot{h} \end{bmatrix}, \quad \ddot{\mathbf{p}} = \begin{bmatrix} \ddot{\rho} \\ \rho\ddot{\sigma} \\ \ddot{h} \end{bmatrix} + \begin{bmatrix} -\rho\dot{\sigma}^2 \\ 2\dot{\rho}\dot{\sigma} \\ 0 \end{bmatrix}, \tag{3}$$

where in the last term $-\rho\dot{\sigma}^2$ is the centripetal acceleration and $2\dot{\rho}\dot{\sigma}$ is the Coriolis acceleration.

2.3 Reference Path/Trajectory on a sphere

A sequence of segments of spherical circles can define a reference path or reference trajectory on the surface of a sphere. Using the motion primitives from the previous section, a path can be represented by a sequence of center points $\{C_1, C_2, C_3, ...\}$, together with transition points $\{p_1, p_2, p_3, ...\}$, or a trajectory can be defined by a timed sequence of center points $C(t) \in \{C_1, C_2, C_3, ...\}$.

By following multiple centers and consistently switching at the same transition point p^*, we arrive at the scenario illustrated in Fig. 3.

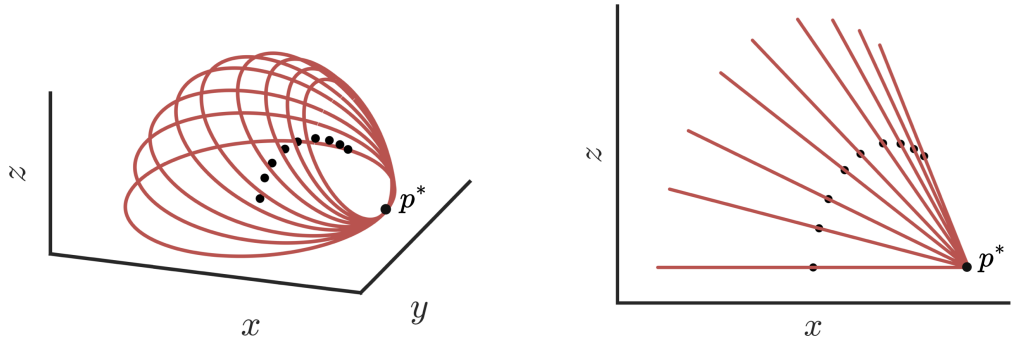

Fig. 3 Set of center points $\{C_1, C_2, C_3, ...\}$ (displayed in black) for transitions occurring at the same point $p*$.

3 Tethered aircraft kinematics and dynamics on the motion primitive

The aircraft position can be expressed in spherical coordinates, (r, φ, β), where r denotes the radial distance, φ the azimuth angle, and β the elevation angle measured from the horizontal plane. The coordinate system is centered at the tether anchorage point, with the associated basis vectors denoted by $(\mathbf{e}_r, \mathbf{e}_\varphi, \mathbf{e}_\beta)$. For additional details, we refer to [6, 11].

3.1 Attitude

The aircraft's attitude is described by the angles of the body coordinate frame with the cylindrical coordinate frame. The body coordinate frame has basis $(\mathbf{e}_X, \mathbf{e}_Y, \mathbf{e}_Z)$, where $\mathbf{e}_X$ is the aircraft's longitudinal axis pointing to its nose, $\mathbf{e}_Y$ is the transversal axis pointing out of the right wing, and $\mathbf{e}_Z$ is the aircraft's vertical axis pointing down from its belly. We define the path-pitch angle, $\underline{\theta}$, and the path-roll angle, $\underline{\phi}$, to be the angles of the $\mathbf{e}_X$ and $\mathbf{e}_Y$ axis, respectively, with the path plane π. The path-yaw angle, $\underline{\psi}$ is the angle between e_σ and the projection of $\mathbf{e}_X$ onto the plane π. When there is no risk of ambiguity with the standard roll, pitch, and yaw, we denote these angles simply by ϕ, θ, ψ without the underline.

3.2 Kinematics

The aircraft's velocity vector is also denoted by $\mathbf{V}$ ($\mathbf{V} = \dot{\mathbf{p}}$), with magnitude V and its angle with the plane π is the flight-path angle $\underline{\gamma}$, or simply denoted by γ when there is no ambiguity with the standard flight-path angle measuring the angle of the velocity vector with the horizontal plane. In this work, we assume that wind is not present, thus the apparent velocity $\mathbf{V}_a$ is equal to $\mathbf{V}$. The kinematics of the aircraft in cylindrical coordinates satisfy

$$
\begin{aligned}
\dot{\rho} &= -V\frac{r_C + h}{r}\sin\gamma \\
\dot{\sigma} &= \frac{V}{\rho}\cos\gamma \\
\dot{h} &= V\frac{\rho}{r}\sin\gamma.
\end{aligned} \tag{4}
$$

3.3 Forces

The aircraft is subject to the following forces (see Fig. 4): the propeller thrust $\mathbf{F}_\mathrm{p} = F_\mathrm{p}\,\mathbf{e}_X$, the weight $\mathbf{F}_g$ with magnitude $m\,g$ pointing down, the aerodynamic lift $\mathbf{F}_\mathrm{L} = F_\mathrm{L}\,\mathbf{e}_\mathrm{L}$, the aerodynamic drag $\mathbf{F}_\mathrm{D} = F_\mathrm{D}\,\mathbf{e}_\mathrm{D}$, the tether pull $\mathbf{F}_\mathrm{t} = -F_\mathrm{t}\,\mathbf{e}_r$, and also the inertial forces $\mathbf{F}_\mathrm{i}$ when a rotating frame is considered.

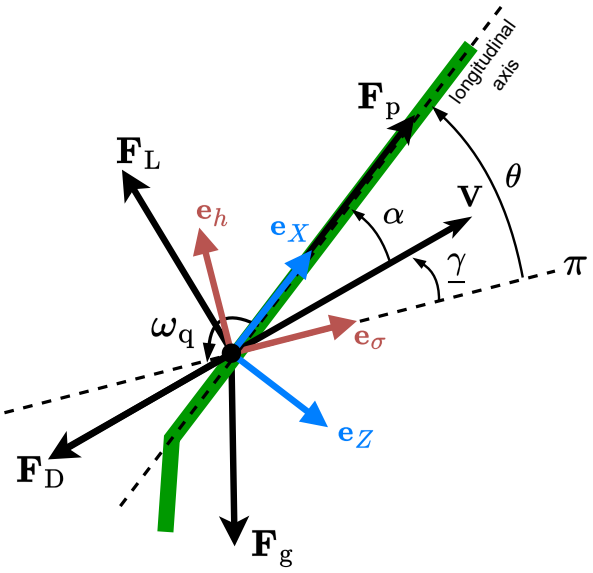

Fig. 4 Airplane longitudinal model (aircraft longitudinal shape colored green)

In the aerodynamic forces, the direction of the drag is given by the unit vector $\mathbf{e}_\mathrm{D}$ which is in the opposite direction of airspeed vector and given by $-\mathbf{v}_a/||\mathbf{v}_a||$; the direction of the lift is given by $\mathbf{e}_\mathrm{L}$, which is equal to $\mathbf{e}_Y \times \mathbf{v}_a/||\mathbf{v}_a||$, perpendicular to the plane defined by $\mathbf{V}_a$ and $\mathbf{e}_Y$. The magnitudes of the aerodynamic forces are given by

$$
F_\mathrm{D} = \frac{1}{2}\rho_a A V_a^2 c_\mathrm{D}(\alpha) \quad \text{and} \quad F_\mathrm{L} = \frac{1}{2}\rho_a A V_a^2 c_\mathrm{L}(\alpha), \tag{5}
$$

where V_a is the magnitude of the airspeed vector $\mathbf{V}_a$, ρ_a is the air density, A is the wing area, and $c_\mathrm{D}(\alpha)$ and $c_\mathrm{L}(\alpha)$ are the drag and lift coefficients, respectively, which vary with the angle of attack α. The inertial forces in the cylindrical coordinate frame are $\mathbf{F}_\mathrm{i} = m\rho\dot{\sigma}^2\,\mathbf{e}_\rho - 2m\dot{\rho}\dot{\sigma}\,\mathbf{e}_\sigma$, due to the centripetal and Coriolis terms. The magnitude of the tether force F_t satisfies $F_t = \mathrm{Proj}_{e_r}\left(\mathbf{F}_\mathrm{L} + \mathbf{F}_\mathrm{D} + \mathbf{F}_\mathrm{p} + \mathbf{F}_\mathrm{g} + \mathbf{F}_\mathrm{i}\right)$.

The total force acting on the aircraft can be written in the cylindrical coordinate frame

$$
F^C = \begin{bmatrix} F_\rho \\ F_\sigma \\ F_h \end{bmatrix} = R_{GC}\left[\mathbf{F}_\mathrm{L} + \mathbf{F}_\mathrm{D} + \mathbf{F}_\mathrm{p} + \mathbf{F}_\mathrm{g} + \mathbf{F}_\mathrm{t} + \mathbf{F}_\mathrm{i}\right], \tag{6}
$$

where R_{GC} is the rotation matrix from global to cylindrical coordinates. The resultant force yields in each component

$$\begin{aligned}
F_\rho =& \cos\alpha \sin\phi\, L + \sin\alpha \sin\phi\, D - \frac{\sqrt{r^2 - r_C^2}}{r} T - gm \cos\beta_c \sin\sigma + \frac{V^2 m \cos^2\gamma}{\rho} \\
F_\sigma =& (\sin\alpha \cos\theta - \cos\alpha \cos\phi \sin\theta)\, L - (\cos\alpha \cos\theta + \cos\phi \sin\alpha \sin\theta)\, D \\
&+ \cos\theta\, F_\mathrm{p} - gm \cos\beta_c \cos\sigma + \frac{2V^2 m \cos\gamma \sin\gamma (h + r_C)}{r\rho} \\
F_h =& (\sin\alpha \sin\theta + \cos\alpha \cos\phi \cos\theta)\, L + (\cos\phi \sin\alpha \cos\theta - \cos\alpha \sin\theta)\, D \\
&- \frac{r_C}{r} T + \sin\theta\, F_\mathrm{p} - gm \sin\beta_c .
\end{aligned} \tag{7}$$

3.4 Dynamics

Differentiating the kinematics (4), we obtain

$$\begin{aligned}
\ddot{\rho} &= -\frac{(h + r_c)\sin\gamma}{r}\dot{V} - \frac{(h + r_c) V \cos\gamma}{r}\dot{\gamma} - \frac{\rho V^2 \sin^2\gamma}{r^2} \\
\ddot{\sigma} &= \frac{\cos\gamma}{\rho}\dot{V} - \frac{V \sin\gamma}{\rho}\dot{\gamma} + \frac{(h + r_c) V^2 \cos\gamma \sin\gamma}{r \rho^2} \\
\ddot{h} &= \frac{\rho \sin\gamma}{r}\dot{V} + \frac{V\rho \cos\gamma}{r}\dot{\gamma} - \frac{(h + r_c) V^2 \sin^2\gamma}{r^2}
\end{aligned} \tag{8}$$

which combining with $m\mathbf{p} = \left[F_\rho \; F_\sigma \; F_h\right]^T$, and solving for $\dot{V}, \dot{\gamma}$, we obtain

$$\begin{aligned}
\dot{V} =& \cos\gamma \left(\frac{F_\sigma}{m} - \frac{(h + r_c) V^2 \cos\gamma \sin\gamma}{r\rho}\right) + \frac{r \sin\gamma \left(\dfrac{F_h}{m} + \dfrac{V^2 \sin^2\gamma\, (h + r_c)}{r^2}\right)}{\rho} \\
\dot{\gamma} =& \frac{r \cos\gamma \left(\dfrac{F_h}{m} + \dfrac{V^2 \sin^2\gamma\, (h + r_c)}{r^2}\right)}{V\rho} - \frac{\sin\gamma \left(\dfrac{F_\sigma}{m} - \dfrac{V^2 \cos\gamma \sin\gamma\, (h + r_c)}{r\rho}\right)}{V}.
\end{aligned} \tag{9}$$

These equations, along with the kinematic relations in (4), define the longitudinal motion model of the tethered aircraft. This model is analogous to the conventional longitudinal model of a fixed-wing aircraft (see [12, 13]), and Fig. 4, with adjustments for circular tethered flight.

We consider that the thrust force F_p, the pitch rate ω_q, and the roll angle ϕ are directly actuated variables. Although thrust and body rates are treated as directly actuated inputs, this does not restrict practical applicability. In a real system, the commanded angular rates and thrust can be tracked by inner-loop PID controllers that map these references to control surface deflections and motor duty-cycle. This standard cascade control structure allows the high-level motion primitive controller to be implemented independently of the specific actuator dynamics.

The resulting state and control vectors considered are

$$\mathbf{X} = \left[\rho, \sigma, h, V, \gamma, \theta\right]^\mathrm{T} \text{ and } \mathbf{U} = \left[F_\mathrm{p}, \omega_q, \phi\right]^\mathrm{T},$$

respectively. The state-space model is given by

$$\mathbf{X} = \left[\dot{\rho}, \dot{\sigma}, \dot{h}, \dot{V}, \dot{\gamma}, \dot{\theta}\right]^{\mathrm{T}} = f(\mathbf{X}, \mathbf{U}),$$

where the dynamic function f is obtained by combining equations (4) for the first three lines, equations (9) for the fourth and fifth lines, and $\dot{\theta} = \omega_q$ for the last line. This is the model that is used in simulations and serves as the basis to deduct other models for controller design.

4 Control Architecture

The main advantage of using the motion primitives framework and the cylindrical coordinate frame is that it becomes an easy task to design a controller to drive the trajectory to a reference path that is in a primitive. This is because the periodic variable σ is almost not present in the dynamics, the only exception being the gravitational force. The dependence of the gravitational force on σ is inevitable since it is not uniform for non-horizontal paths. A main consequence is that a simple linearized model around a point in the path is a good approximation near the reference path. This benefit is even more evident when the gravitational force is small when compared to the other actuating forces, as is frequently the case. Thus, a simple Linear Quadratic Regulator (LQR) for each primitive yields good results when considering the 4 components reduced state

$$x = [h, V, \gamma, \theta]^T,$$

with the control

$$u = \mathbf{U} = \left[F_{\mathrm{p}}, \omega_q, \phi\right]^{\mathrm{T}}.$$

To design the controller for each primitive path, given the path center coordinates, we start by determining an equilibrium state for trimmed steady flight in which $(\dot{h}, \dot{V}, \dot{\gamma}, \dot{\theta}) = (0, 0, 0, 0)$ for $\alpha = 0, h = 0, \gamma = 0, \theta = 0, \phi = 0, \sigma = 0$, yielding reference values $V^{\mathrm{ref}}, F_{\mathrm{p}}^{\mathrm{ref}}$. Then, we linearize around $(x^{\mathrm{ref}}, u^{\mathrm{ref}})$ and control the error process $(\tilde{x}, \tilde{u}) = (x, u) - (x^{\mathrm{ref}}, u^{\mathrm{ref}})$ with linear dynamics $\dot{\tilde{x}} = A\tilde{x} + B\tilde{u}$ where A and B are the Jacobian linearization matrices. The objective function of the LQR $\int_0^\infty \left(\widetilde{\mathbf{x}}^T Q \widetilde{\mathbf{x}} + \widetilde{\mathbf{u}}^T R \widetilde{\mathbf{u}}\right) dt$, is defined by two weight matrices, Q and R, which are initially set to be diagonal matrices and then manually adjusted according to the desired response. The values of the weight matrices used, as well as the values of the reference points for each simulation are described in the next section.

To follow a desired complex path on the surface of a sphere, we need to switch between path primitives, implying switching between controllers, which might lead to undesired behaviors. Smooth transitions and continuous curvatures are obtained when following smooth pasting condition: when transitioning from center C_1 to C_2 at position p, the velocity vector $\overrightarrow{V}$ should be orthogonal to the lines going from p to both the centers, that is

$$\begin{aligned} (C_1 - p) \cdot \overrightarrow{V} &= 0, \\ (C_2 - p) \cdot \overrightarrow{V} &= 0. \end{aligned} \tag{10}$$

This condition is respected in the examples explored below.

5 Simulation and Results

This section presents the outcomes of simulations conducted to validate the proposed control architecture utilizing motion primitives for a tethered aircraft. Table 1 provides an overview of the aircraft and

simulation parameters, which follow our previous work related to take-off and landing of tethered aircraft [4, 6, 11]. Table 2 reports the values of the reference states and weight matrices used in the simulation for each primitive. The table includes the elevation angles for each center C, following the work [9].

Table 1 Aircraft and Simulation Parameters

$A = 0.0720\,\mathrm{m}^2$, $m = 0.350\,\mathrm{kg}$
$b = 0.60\,\mathrm{m}$, $r = 30b = 18\,\mathrm{m}$
$F_\mathrm{p} \in [0; 6]\,\mathrm{N}$, $\omega_q \in [-20; 20]^\circ\ \mathrm{s}^{-1}$, $\phi \in [-10; 10]^\circ$
$\rho = 1.225\,\mathrm{kg\,m}^{-3}$, $g = 9.8\,\mathrm{m\,s}^{-2}$, $V_w = 0\,\mathrm{m\,s}^{-1}$

Table 2 Controller references, gains, and objectives for each motion primitive

Elevation Angles
$\beta_0 = \arcsin\left(\frac{2b}{r}\right)$
$\beta_1 = \pi/2, \quad \beta_2 = \pi/3, \quad \beta_3 = \pi/4$
Loiter with center $C_1 = (2b, 0, \beta_1)$
$(h, V, \gamma, \theta)_\mathrm{ref} = (0, 8.64, 0, 0)$
$Q = \mathrm{diag}([50\ \ 10\ \ 10\ \ 200])$
$R = \mathrm{diag}([1\ \ 100\ \ 100])$
Loiter with center $C_2 = (r\cos(\beta_2 - \beta_0), 0, \beta_2)$
$(h, V, \gamma, \theta)_\mathrm{ref} = (0, 9.69, 0, 0)$
$Q = \mathrm{diag}([100\ \ 10\ \ 10\ \ 200])$
$R = \mathrm{diag}([1\ \ 100\ \ 100])$
Loiter with center $C_3 = (r\cos(\beta_3 - \beta_0), 0, \beta_3)$
$(h, V, \gamma, \theta)_\mathrm{ref} = (0, 13.38, 0, 0)$
$Q = \mathrm{diag}([100\ \ 10\ \ 10\ \ 200])$
$R = \mathrm{diag}([1\ \ 100\ \ 100])$

The controllers were implemented using MATLAB/Simulink, and the simulation results for both cases are presented in Fig. 5 and 6, for the state variables and control inputs, respectively. In the first figure, from top to bottom, it is displayed the cylindrical coordinates (ρ, σ, h), then the kite speed and finally, at the bottom, the attitude angles: pitch angle, angle-of-attack, and flight path angle (shown in blue, red, and green). In the control graphs, we can see the propeller force, pitch angular rate and roll angle. The initial ρ defined for the simulation is 0.5 m below the reference, which corresponds to around 3 m above h_ref.

The overall simulation results show that the controller is capable of following the predefined references for h, γ and θ, with only small variations. As a consequence, the radial cylindrical component reference - ρ_ref, which corresponds to the radius of each primitive, although not explicitly considered in the design of the controller, is closely followed as well. The speed profile does not follow the speed reference in the two non-horizontal circles, since the speed reference was computed setting $\sigma = 0$. This

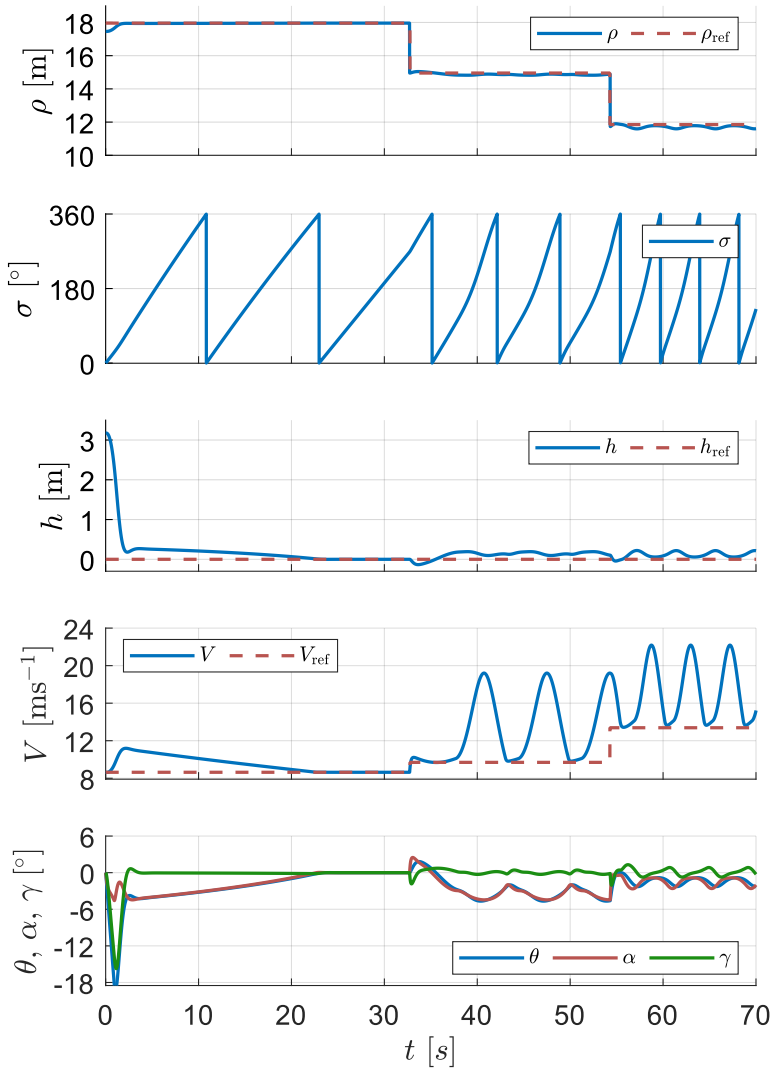

Fig. 5 Simulation results for the state variables $\mathbf{X} = \left[\rho, \sigma, h, V, \gamma, \theta\right]^{\mathrm{T}}$.

variation can be justified by the effect of gravity. The aircraft tends to accelerate during the descent part of the path, even setting the propeller force to zero. During the ascent part of the path, the kite tends to slow down, thus requiring a boost from the propeller. The system was trimmed with $\sigma = 0$, which corresponds to the ascending and thus, slower part of the path. This led to guarantee the minimum speed required to successfully complete the climb. Due to the decrease of each center elevation angle, and the increase of r_C, the radius of each circle decreases and the aircraft speed increases. Consequently, the lap time of each primitive decreases, as depicted by σ.

In Fig. 7 is displayed a 3D simulation result. It provides a visualization of the predefined circles of motion, with centers $\{C_1, C_2, C_3\}$. The trajectory described by the kite during the simulations is displayed with a blue line. The initial position for the simulation is represented with a ball. The kite can actively follow the predefined curves, with smooth transitions occurring around the point where $\sigma = 270°$, as mentioned earlier. Finally, Fig. 8 shows a 3D plot with the body frame of the tethered aircraft during the simulation. The body coordinate frame basis $(\mathbf{e}_x, \mathbf{e}_y, \mathbf{e}_z)$ is represented in red, green, and blue colors, respectively. The plotted kites are not to scale.

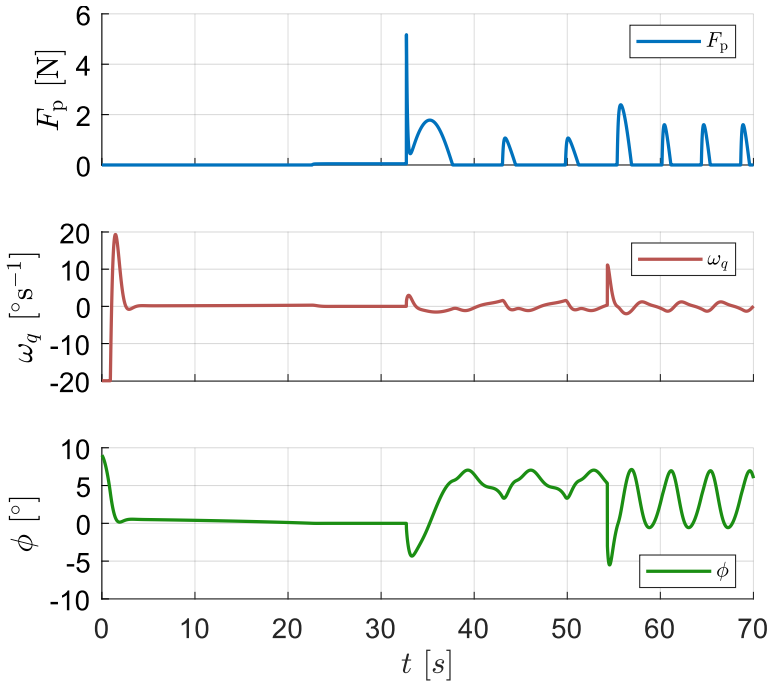

Fig. 6 Simulation results for the control variables $\mathbf{U} = \left[F_{\mathrm{p}}, \omega_q, \phi\right]^{\mathrm{T}}$.

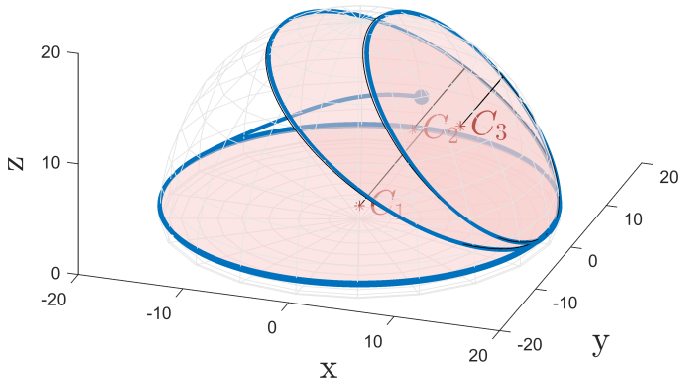

Fig. 7 3D simulation result.

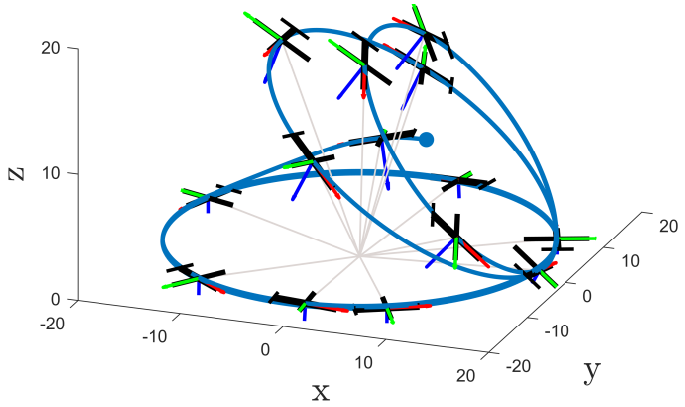

Fig. 8 3D simulation with tethered aircraft body.

6 Conclusion

This study underscores the effectiveness of motion primitives in control design for tethered aircraft. The paper highlights the advantages of employing the motion primitives framework in conjunction with cylindrical coordinates. This approach simplifies controller design to guide the trajectory towards a reference path within a given primitive. The simplification is due to the fact that the periodic variable σ has minimal influence on system dynamics. Consequently, a linearized model around a point on the reference path provides an accurate local approximation, facilitating the application of standard linear multivariable control techniques along each motion primitive. The simulation results demonstrate that the proposed controller, which integrates the motion primitive framework with a cylindrical coordinate system, effectively tracks predefined reference values with minimal deviations. A smooth transition between motion primitives and controllers is achieved through compliance with the smooth pasting condition of the velocity vectors. Overall, the simulated aircraft consistently follows the intended circular motion trajectories, exhibiting smooth transitions between motion segments.

Acknowledgments

This work is financially supported by Project 2022.02801.PTDC-UPWIND-ATOL (https://doi.org/10.54499/2022.02801.PTDC), as well as by grants 2021.06313.BD and 2021.07346.BD, and by the SYSTEC – Research Center for Systems and Technologies (UID/00147) and the Associate Laboratory ARISE – Advanced Production and Intelligent Systems (LA/P/0112/2020, DOI: 10.54499/LA/P/0112/2020), all funded by Fundação para a Ciência e a Tecnologia, I.P./MECI through national funds.

References

[1] Miguel Nakajima Marques, Sandro Augusto Magalhães, Filipe Neves Dos Santos, and Hélio Sousa Mendonça. Tethered Unmanned Aerial Vehicles—A Systematic Review. *Robotics*, 12(4):117, Aug. 2023. ISSN: 2218-6581. Number: 4 Publisher: Multidisciplinary Digital Publishing Institute. DOI: 10.3390/robotics12040117.

[2] Roland Schmehl, editor. *Airborne Wind Energy: Advances in Technology Development and Research*. Green Energy and Technology. Springer, Singapore, 2018. ISBN: 978-981-10-1946-3 978-981-10-1947-0. DOI: 10.1007/978-981-10-1947-0.

[3] Chris Vermillion, Mitchell Cobb, Lorenzo Fagiano, Rachel Leuthold, Moritz Diehl, Roy S. Smith, Tony A. Wood, Sebastian Rapp, Roland Schmehl, David Olinger, and Michael Demetriou. Electricity in the air: Insights from two decades of advanced control research and experimental flight testing of airborne wind energy systems. *Annual Reviews in Control*, 52:330–357, Jan. 2021. ISSN: 1367-5788. DOI: 10.1016/j.arcontrol.2021.03.002.

[4] Sérgio Vinha, Gabriel M. Fernandes, Huu Thien Nguyen, Manuel C.R.M. Fernandes, and Fernando A.C.C. Fontes. Automatic Circular Take-off and Landing of Motorized Tethered Aircraft. In *2024 European Control Conference (ECC)*, pages 681–686, June 2024. DOI: 10.23919/ECC64448.2024.10590893, `https://ieeexplore.ieee.org/document/10590893`.

[5] Sérgio Vinha, Gabriel M. Fernandes, and Fernando A. C. C. Fontes. A Discussion on Automatic Take-off and Landing Approaches for Airborne Wind Energy Systems. In *Book of Abstracts of the International Airborne Wind Energy Conference 2024*, Madrid, Spain, Apr. 2024. `https://repository.tudelft.nl/islandora/object/uuid%3A4593e793-a10b-47ab-8c34-a3bef0886461`.

[6] Sérgio Vinha, Gabriel Fernandes, Manuel Fernandes, Huu Nguyen, and Fernando A. C. C. Fontes. Control of Fixed-Wing Tethered Aircraft in Circular Take-Off and Landing Maneuvers. In *Proceedings of ICINCO24 - 21st International Conference on Informatics in Control, Automation and Robotics*, pages 319–326, Nov.

2024. ISBN: 978-989-758-717-7. DOI: 10.5220/0013067000003822, https://www.scitepress.org/PublicationsDetail.aspx?ID=p/pIyovVGfs=&t=1.

[7] Aditya A. Paranjape, Kevin C. Meier, Xichen Shi, Soon-Jo Chung, and Seth Hutchinson. Motion primitives and 3D path planning for fast flight through a forest. *The International Journal of Robotics Research*, 34(3):357–377, Mar. 2015. ISSN: 0278-3649. Publisher: SAGE Publications Ltd STM. DOI: 10.1177/0278364914558017.

[8] Qianyi Fu, Jun Li, and Wenjie Zhao. Motion primitives and sample-based trajectory planning for fixed-wing unmanned aircraft. *Transactions of the Institute of Measurement and Control*, page 01423312241264873, Sept. 2024. ISSN: 0142-3312. Publisher: SAGE Publications Ltd STM. DOI: 10.1177/01423312241264873.

[9] Sérgio Vinha, Gabriel M. Fernandes, Manuel C.R.M. Fernandes, and Fernando A.C.C. Fontes. Motion Primitives on a Spherical Surface with Application to Tethered Aircraft Guidance. In *2025 IEEE 19th International Conference on Control & Automation (ICCA)*, pages 186–191, June 2025. ISSN: 1948-3457. DOI: 10.1109/ICCA65672.2025.11129856, https://ieeexplore.ieee.org/abstract/document/11129856.

[10] KF Riley, MP Hobson, and SJ Bence. *Mathematical Methods for Physics and Engineering*. Cambridge University Press, 2006.

[11] Gabriel M. Fernandes, Sérgio Vinha, Manuel C.R.M. Fernandes, and Fernando A.C.C. Fontes. Control of circular take-off in tethered aircraft under wind. In *11th IFAC Symposium on Robust Control Design (ROCOND 2025)*, july 2025.

[12] Huu Thien Nguyen, Ionela Prodan, and Fernando A. C. C. Fontes. Trajectory Optimization and NMPC Tracking for a Fixed–Wing UAV in Deep Stall with Perch Landing. In *2023 European Control Conference (ECC)*, pages 1–7, June 2023. DOI: 10.23919/ECC57647.2023.10178188.

[13] Randal W. Beard and Timothy W. McLain. *Small Unmanned Aircraft*. Princeton, 2012. ISBN: 978-0-691-14921-9.